

pubs.acs.org/JPCL Letter

# Imaging Infrared Plasmon Hybridization in Doped Semiconductor Nanocrystal Dimers

Agust Olafsson, Siamak Khorasani, Jacob A. Busche, Jose J. Araujo, Juan Carlos Idrobo, Daniel R. Gamelin, David J. Masiello,\* and Jon P. Camden\*



Cite This: J. Phys. Chem. Lett. 2021, 12, 10270-10276



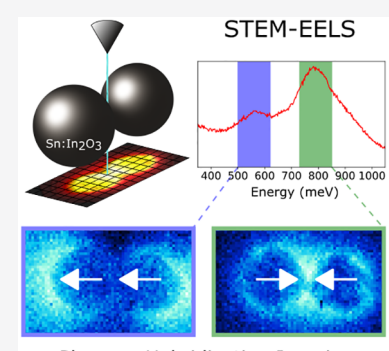
**ACCESS** 

III Metrics & More

Article Recommendations

s Supporting Information

ABSTRACT: Carrier-doped semiconductor nanocrystals (NCs) offer strong plasmonic responses at frequencies beyond those accessible by conventional plasmonic nanoparticles. Like their noble metal analogues, these emerging materials can harness free space radiation and confine it to the nanoscale but at resonance frequencies that are natively infrared and spectrally tunable by carrier concentration. In this work we combine monochromated STEM-EELS and theoretical modeling to investigate the capability of colloidal indium tin oxide (ITO) NC pairs to form hybridized plasmon modes, providing an additional route to influence the IR plasmon spectrum. These results demonstrate that ITO NCs may have greater coupling strength than expected, emphasizing their potential for near-field enhancement and resonant energy transfer in the IR region.



Plasmon Hybridization Imaging

Localized surface plasmons (LSPs) concentrate optical energy into spatial regions significantly smaller than the diffraction limit. How well understood at visible frequencies, plasmonic responses in the infrared (IR) region are more difficult to achieve, despite being of considerable interest for applications in communications, hency harvesting, molecular sensing, have and surface-assisted photocatalysis. Molecular sensing, have a semiconductors offer a new class of nanomaterials with native IR LSP resonances that are tunable by controlling the free carrier concentrations via chemical doping strategies. As a result, the IR response properties of these semiconductor nanomaterials and nanocrystals (NCs) are the subject of intense recent efforts. 16,21–25

The emergent properties of interacting nanostructures are key elements that define the characteristics of the LSP's electromagnetic field, 1,2 and plasmon hybridization can be employed to tune the spectrum of interacting particles. When in close proximity, the LSPs of individual particles can mix and form new hybridized plasmons with energies and spatial distributions dictated by the coupling strength and detuning of the individual particle responses. 26,27 Furthermore, LSPs can be simultaneously coupled to different and competing energy dissipation pathways or hybridize with other resonant modes in the local environment. 28-30 This variety of interactions presents a challenge for understanding how energy transfer occurs in nanoscale plasmonic materials. Although plasmon hybridization is well studied in noble metal nanoparticles, <sup>26,30–32</sup> it is unclear if NC particles meet the conditions necessary to undergo equivalent hybridization and coupling.<sup>1,2,4</sup> Particularly, no previous studies have explored how the range of LSP energies and dielectric parameters of NCs<sup>22,24</sup> influence the coupling strength and mixing parameters in fewparticle systems. While recent works have examined plasmons of NC bulk aggregates<sup>33,34</sup> and the IR LSPs of NC clusters,<sup>34,35</sup> a clear picture of the effects of these parameters, as well as doping effects, has yet to emerge.

Thus, to better understand and apply NC plasmons for IR applications, it is critical that we characterize the near-field electromagnetic profiles and interactions within few-particle clusters of NCs, as their hybridization capabilities are encoded within these results. Scanning transmission electron microscopy—electron energy loss spectroscopy (STEM-EELS) has the ability to directly measure the near-field resonances of plasmons at the nanoscale. The electromagnetic field induced by a focused STEM electron beam behaves like an evanescent white light source, relaxing common far-field optical selection rules and enabling the excitation of the complete set of LSP modes of a plasmonic particle. Importantly, the resulting plasmon excitations cause electron scattering interactions that can be energy-separated and measured in EELS to determine the resonance features of a nanomaterial. Recent advancements in electron energy monochromation have pushed EELS

Received: August 20, 2021 Accepted: October 8, 2021 Published: October 15, 2021





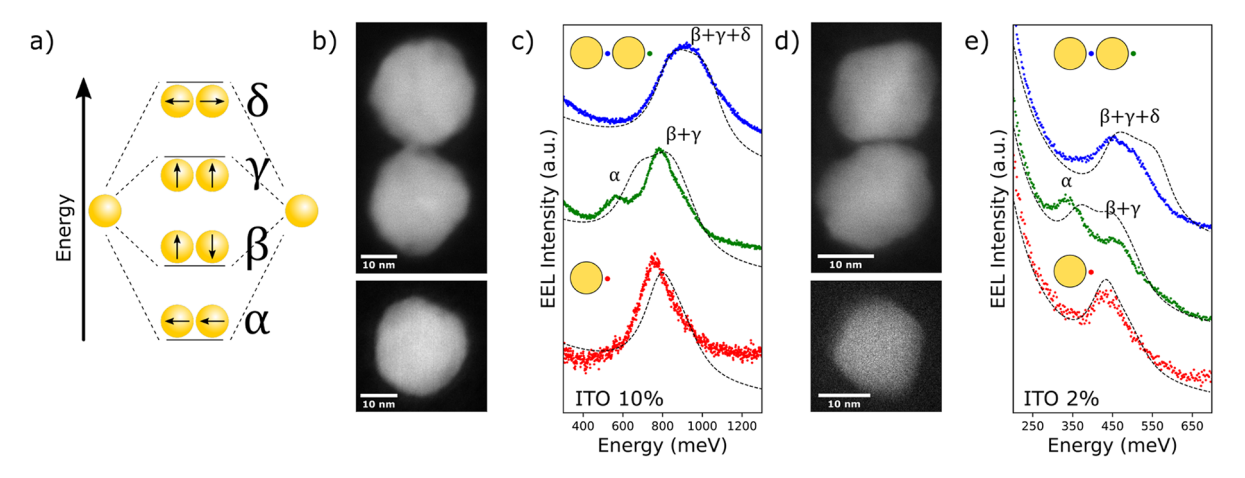


Figure 1. Surface plasmon hybridization of ITO NC dimers. The hybridization diagram (a) depicts the collinear in-phase ( $\alpha$ ), perpendicular in-phase ( $\beta$ ), perpendicular out-of-phase ( $\beta$ ), ocupled modes. TEM images of the 10% Sn<sup>4+</sup> (b) and 2% Sn<sup>4+</sup> (d) doped ITO NC samples studied. Experimental EEL point spectra (c, e) collected at the aloof positions of the monomer (red), dimer end (green), and dimer gap (blue) together with corresponding simulated EEL spectra (black dash). The rising feature at low energy is the zero loss peak tail (Supporting Information).

measurements into the far-IR, providing new utility for the measurement of IR plasmonic materials. As a result, recent STEM-EELS experiments have characterized the spectral tunability of IR LSPs in doped NCs at the single particle level 22,24 and revealed that NCs exhibit geometric LSP modes with independent energy signatures that are analogous to metals. Additionally, hybrid modes of semiconductor NCs have been extracted from EELS maps of 3–4 particle fluorine—ITO clusters using multivariate analysis; however, to date no studies have examined the hybrid modes of spherical NC dimers.

In this work, we examine the hybridization of indium tin oxide (ITO) NC dimers using STEM-EELS. A combined experimental and theoretical approach details the hybridization of 2% and 10% tin-doped ITO NC dimers, while we additionally extend the theoretical work to study the IR responses of ITO dimers with tin doping concentrations down to 1%. By restricting the analysis to the dipolar surface plasmon limit for 20 nm spherical NCs, we demonstrate hybridization of NCs proceeds in a similar fashion to that of noble metals. Taken together our experimental and theoretical results offer new strategies to tailor the plasmonic properties of NC materials in the IR beyond that of carrier doping.

Figure 1a illustrates the hybridized LSP modes of a dimer and their relative energies:  $\alpha$  and  $\delta$  are the in-phase and out-ofphase collinear LSP modes, while  $\beta$  and  $\gamma$  are the in-phase and out-of-phase perpendicular LSP modes. The latter are each doubly degenerate in the absence of a substrate. Figures 1b and 1d present high-angle annular dark field (HAADF) images of 10% Sn<sup>4+</sup> and 2% Sn<sup>4+</sup> doped ITO NC monomers and dimers. Particle-substrate interactions are minimized by dropcasting a dilute colloid solution onto a 5 nm thick silicon nitride TEM grid, resulting in a stochastic aggregation and orientation of NCs. Once set, NCs are stripped of their oleate ligands<sup>42</sup> to reduce plasmon damping and yield dimers with a gap distance of  $\sim$ 1 nm. We restrict our analysis to particles that are  $\sim$ 20 nm in diameter and are at least 100 nm separated from nearby particles to ensure the collected spectra are not contaminated by other resonances.<sup>36,43</sup> We additionally take care to select mostly spherical particles due to the sensitive nature of the LSP responses to nanoparticle geometry.

Figures 1b and 1c show the experimentally measured STEM annular dark field (ADF) images and corresponding EEL spectra of an ITO NC monomer and dimer with 10% tin doping. The monomer spectrum (red) has a single peak at 770 meV corresponding to the three degenerate dipolar LSPs.<sup>24</sup> The aloof spectrum acquired at the dimer end (green) exhibits features at 565 and 800 meV. Based on the analogy to noble metal dimers, <sup>26,27</sup> the lowest energy peak is associated with the strongest plasmonic coupling, which occurs along the longitudinal axis of the dimer  $(\alpha)$ . The higher energy peak is dominated by a combination of  $\beta$  and  $\gamma$  modes, with the  $\delta$ mode being only weakly excited from this beam position. The aloof spectrum acquired in the gap (blue) shows a broad resonance feature with a peak maximum of ~900 meV partially overlapping the higher energy resonance acquired at the dimer end (green). This broad resonance feature is expected to be composed of both in-phase  $(\beta)$  and out-of-phase  $(\gamma)$ perpendicular modes as well as the out-of-phase collinear mode  $(\delta)$ ; however, definitive assignment based on the measured point spectra is difficult due to spectral overlap of the resonances features and is only revealed in the spectrum images (vide infra, Figure 2). The disappearance of the lowest energy feature  $(\alpha)$  in the gap spectrum (blue) due to selection rules does confirm its assignment as the collinear in-phase  $\alpha$ mode. 1,36,44

Figures 1d and 1e show the experimentally measured STEM ADF images and the corresponding EEL spectra of an ITO NC monomer and dimer with 2% tin doping. The same probe positions are used for the spectra in Figure 1e as in Figure 1c. At the 2% Sn<sup>4+</sup> dopant level, the bulk plasmon is lower in energy when compared to the 10% Sn<sup>4+</sup>, <sup>24</sup> and this difference directly contributes to the difference in the surface plasmon energies observed. The aloof spectra of the 2% ITO monomer (red) has a feature at 440 meV that corresponds to the dipolar LSP, which is ~300 meV lower in energy compared to the same dipolar LSP mode of the 10% ITO monomer. Hybridization of the 2% ITO dimer occurs in a manner identical with that of the 10% dimer, with two features present in the dimer end spectrum (green) and a broad composite peak in the gap spectrum (blue). The relative intensity of the 2% peaks and their proximity to the zero loss peak (ZLP) tail

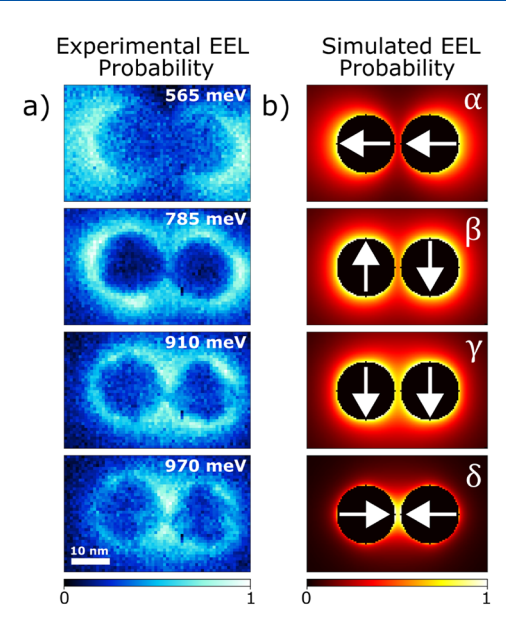


**Figure 2.** EEL spectrum images displaying IR plasmon hybridization in a 10% ITO NC dimer. The experimental (a) and simulated (b) images demonstrate each of the four hybrid dipolar modes  $(\alpha, \beta, \gamma,$  and  $\delta)$ . The subtle difference between perpendicular modes  $\beta$  and  $\gamma$  is indicated by the node of low probability in the  $\beta$  mode junction that is absent in the  $\gamma$  mode junction.

make determining the exact contributions of  $\beta$ ,  $\gamma$ , and  $\delta$  more difficult, but the  $\alpha$  peak is clearly recognizable at 345 meV. These results demonstrate that regardless of the Sn<sup>4+</sup> dopant concentration, which corresponds to the number of free carriers,<sup>22</sup> ITO NCs are capable of forming hybrid plasmon modes analogous to noble metal nanoparticles. Moreover, these LSPs will hybridize at energies well into the low-loss regime, highlighting their potential as IR-active nanomaterials.

By use of the dielectric Drude parameters extracted from STEM-EELS-based nanoellipsometry of individual ITO NCs,<sup>24</sup> numerical EELS simulations (black dash) are displayed in Figures 1c and 1e (Methods). A power-law convolution 44 of the ZLP tail (Supporting Information) has been added to the simulated inelastic scattering spectra to aid the comparison. Differences between simulated and experimental spectra may arise from three different mechanisms: (1) the NC simulations are performed on perfect spheres while the experimentally measured NCs are not perfectly spherical and possess facets (Figure 1b,d); (2) the uncertainty in the underlying ITO dielectric data<sup>24</sup> is greater than that of noble metals; <sup>45</sup> (3) the simulated NCs are modeled in a vacuum environment while the experimental NCs are supported by an amorphous 5 nm thick SiN TEM grid. Substrate-induced image effects are well understood to induce resonance energy shifts and mode mixing<sup>36,37</sup> which would further impact the peak splitting.<sup>46,47</sup> Such faceting and substrate effects were not explicitly modeled herein as our focus lies mainly on qualitative identification of the hybrid NC LSP modes and not on their precise quantitative energies and splittings.

Beyond the point spectra displayed in Figure 1, spectrum imaging allows for the collection of EEL spectra over a region of interest in space, resulting in a hyperspectral data set of positional coordinates, loss energies, and associated EEL probabilities. From this information, the near-field spatial distribution of the EEL probability can be extracted at a specific loss-energy value, thereby providing an image of the

NC dimer's hybridized plasmon modes. For traditional noble metal nanoparticles, such as a dimer of silver nanospheres, the four relevant hybrid modes from Figure 1a have been observed and are well understood. 26,27,32,48 Although previous studies used non-negative matrix factorization to extract hybrid plasmon modes from EELS maps, 35,49 to date no combined theoretical and experimental studies have identified hybrid modes in coupled semiconductor NC dimers. Therefore, Figure 2 displays the first spectrum images of the abovementioned hybrid dipolar LSP modes of the 10% tin doped ITO NC dimer. Although we attempted to obtain EEL spectrum images of the 2% sample dimers, pollution by the ZLP and aberrations from the STEM monochromation, 39,40 coupled with the weaker and lower-energy EEL response of the 2% dimers, made interpretation of the resulting images difficult. Together with point spectra, these experimental (a) and theoretical (b) spectrum images confirm the mode assignment in Figure 1.

The hybrid plasmon modes of the 10% ITO NC dimer are identified by comparing the intensity (probability) and nodal structures of the respective EEL spectrum images between experiment (Figure 2a) and simulation (Figure 2b). The 565 meV resonance is established as the collinear in-phase mode by comparing the top two panels. An increased EEL probability at the ends of the NC's long-axis is characteristic of the  $\alpha$  mode, as is the node of low probability in the junction between the two NCs. The  $\beta$  mode in Figure 2, observed experimentally at 785 meV, also has nodal structure between the two particles. However, there is a noticeable increase in EEL probability along the perpendicular short-axis of the NC dimer. The  $\beta$ mode can be differentiated from the  $\gamma$  mode at 910 meV by comparing the nodal structure. This out-of-phase mode has higher EEL intensity in the junction and a slight decrease along the long-axis ends of the dimer. Finally, the highest energy resonance is the out-of-phase collinear  $\delta$  mode at 970 meV, recognizable by the high EEL probability in the junction between the two NCs and low probability at the ends of the dimer. These results demonstrate that NCs exhibit LSP hybridization behavior equivalent to their noble metal analogues, despite their significantly lower resonance energies.

Continued development of controlled geometric NC synthesis will advance the ability to localize infrared energy at the nanoscale via the local fields of such hybrid plasmon modes. We now compare the local electric field enhancements for ITO dimers of varying tin concentration with the field enhancements obtained from a nanoparticle dimer of silver using the tin-concentration-dependent Drude dielectric parameters for ITO established in ref 24 and the tabulated Johnson—Christy dielectric data for silver. Figure 3a shows the progression of calculated near-field enhancements

$$\frac{|\mathbf{E}|}{|\mathbf{E}_{0}|} = 2\left(\frac{a}{r}\right)^{3} \left| \frac{\varepsilon_{\infty} - \frac{\omega_{p}^{2}}{\omega^{2} + i\gamma\omega} - 1}{\varepsilon_{\infty} - \frac{\omega_{p}^{2}}{\omega^{2} + i\gamma\omega} + 2} \right|$$

$$\frac{\omega = \omega_{0}}{\omega_{0}} 2\left(\frac{a}{r}\right)^{3} \frac{\sqrt{(\varepsilon_{\infty} - 1)^{2} + (3\omega_{p}/\gamma)^{2}}}{\varepsilon_{\infty} + 2} \tag{1}$$

under plane-wave excitation for an a=10 nm sphere monomer as a function tin doping concentration versus silver, each evaluated at their respective dipolar LSP resonance. Here,  $\omega_0 = \omega_p/\sqrt{\varepsilon_\infty + 2}$  is the dipolar LSP resonance frequency, r

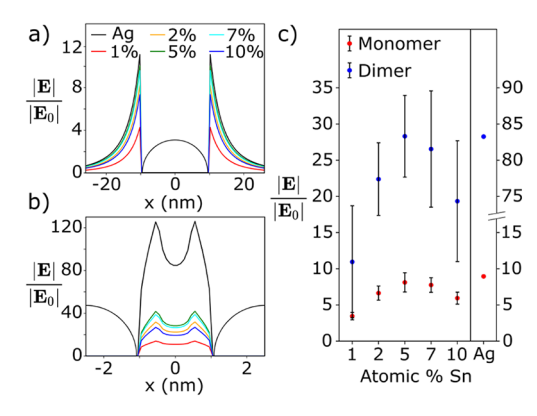


Figure 3. Simulated electric field enhancement in ITO NCs as a function of tin dopant concentration. Line scans show the maximum field enhancement for an ITO monomer (a) and dimer (b) compared to silver, each computed at its respective resonance energy. For both ITO monomers and dimers, the maximum field enhancement occurs at 5% tin doping. ITO field enhancements (c) evaluated at the monomer surface and dimer junction center display this trend and are compared to silver (right column) using a separate magnitude scale. Error bars indicate the standard deviation from the mean values reported in ref 24.

is the radial distance along the incident polarization direction, and  $\varepsilon_{\infty}$ ,  $\gamma$ , and  $\omega_{\nu}$  are the three Drude parameters with the latter scaling as the square root of carrier concentration. It is interesting to note that 5% tin doping provides the largest field enhancement for ITO and that it is comparable to that of silver. Unexpectedly, the calculations also show that the 2% ITO has a field enhancement comparable to that of the 10% ITO. Despite the increased carrier concentration and plasma frequency of the 10% NCs, we attribute this behavior to the reduced damping rate ( $\gamma$ ) of the 2% NCs.<sup>24</sup> Indeed, eq 1 makes explicit how the resonant field enhancement increases with decreasing damping rate. These results illustrate the impacts of the Drude parameters on the near-field enhancement of the particles, demonstrating how carrier concentration is not the only factor that should be considered when comparing different dopant levels in ITO NCs. Our findings stand in contrast to a recent finite element study finding conventional metals have an order of magnitude greater enhancement when compared to NCs, 50 suggesting additional work is needed.

A similar trend is observed in the ITO and silver dimer calculations shown in Figure 3b, though a much larger electric field is produced in the junction between the pair of a = 10 nm particles. Here, we see that the ITO junction field magnitude is slightly less than half that of the silver nanoparticle dimer with a maximum occurring for the 5% ITO dimer as in the case of the monomer. The monomer and dimer trends can be compared directly in Figure 3c, which shows the maximum field at the surface of the monomer surface in Figure 3a and the gap between the dimer in Figure 3b. As described above, the maximum enhancement as a function of dopant concentration is found to be the largest for the 5% ITO NCs; however, all particles show a field enhancement on the same order of magnitude as silver. Despite these more modest enhancements, we note that they are still significantly larger than the incident field strength ( $|\mathbf{E}_0|$  in eq 1) and occur at IR frequencies, making ITO NC dimers good candidates for many plasmonic applications requiring field enhancement at low energies.

While experimental verification of these predictions will be needed to test their validity, LSP coupling strengths can be read directly off of the dimer EEL spectra in Figure 1c,e for both experiment and simulation. Specifically, the splitting between the in-phase ( $\alpha$ ) and out-of-phase ( $\delta$ ) collinear LSP modes is a qualitative measure of coupling strength,  $g = |\hbar\omega_{\alpha} - \hbar\omega_{\delta}|$ . Alternatively, the coupling strength can be calculated analytically in the quasi-static limit for a pair of coupled dipoles as  $g = (2e^2/s^3)/m_0\omega_0$ , where  $m_0 = e^2(\varepsilon_\infty + 2)^2/3\omega_p^2a^3$  is the dipolar LSP effective mass<sup>37,51</sup> and s is the separation distance between the dipoles. Table 1 lists experimental, simulation, and

Table 1. Coupling Strengths of 2% ITO, 10% ITO, and Silver Dimers

coupling strength (meV)	$g_{2\%}$	g <sub>10%</sub>	$g_{ m Ag}$
experiment	169	405	
simulation (e-DDA)	165	200	318
theory (quasi-static)	85	153	363.5

quasi-static theoretical values of g. Because we did not perform EELS measurements on spherical a=10 nm silver dimers, only the simulated and theoretical values are listed; the latter uses the Drude parameters  $\hbar\omega_p=9.326$  eV,  $\hbar\gamma=0.1619$  eV, and  $\varepsilon_\infty=4.519$  to approximate the measured dielectric function of silver.  $^{45}$  From these estimates it is clear that both simulation and theory underestimate the apparent observed coupling strengths. This is likely due to the fact that radiation damping and the presence of higher-order LSP modes are missing from the quasi-static theory, while substrate-induced mode mixing and NC faceting are absent from both theory and simulation. Nevertheless, it is clear that the ITO coupling strengths are comparable to that of silver, which is a surprising result.

In this work we have characterized the resonant IR responses of individual dimers of spherical ITO NCs as a function of carrier concentration for the first time. Our results show that high-resolution STEM-EELS has the ability to spectrally resolve the dimer's hybrid plasmon modes at IR energies with nanometer precision, identifying their unique spatial mode profiles. On the basis of electromagnetic simulations parametrized by our measurements, we show that hybrid IR NC plasmons have robust electric field enhancements like their noble metal analogues, delivering local field strengths within an order of magnitude of silver. Characterization of these plasmonic properties is an important step for the development of NCs with native IR activity, and this research opens several new avenues for using NC hybridization and carrier doping to influence the far-field and local plasmonic responses.

### METHODS

# Doped Semiconductor Nanocrystal Preparation.

Nanocrystalline ITO colloids were grown to a size of  $\sim$ 20 nm diameter by using a previously reported method. This established method yields uniform dopant distributions in NCs and is known to produce NC compositions that match the nominal composition. Diluted colloid solutions were then dropcast onto 5 nm thick amorphous SiN TEM grids, spontaneously forming few particle aggregates such as dimers. NCs were stripped of the oleate ligands by gently bathing the TEM sample in an acetonitrile solution of  $(Et_3O)BF_4$ .

**STEM-EELS Characterization.** Imaging and low-loss EELS measurements were conducted by using a Nion

HERMES monochromated and aberration-corrected STEM-EELS instrument operated at 60 kV accelerating voltage. Highangle annular dark field (HAADF) images of dimers were collected prior to EELS characterization, ensuring that each dimer had a minimum separation distance of 100 nm from nearby particles. All point spectra and EELS maps were acquired with a convergence angle of 30 mrad, a collection angle of 20 mrad, and a beam current of ~10 pA.38-40 Scattered electrons are dispersed in a Nion Iris spectrometer at 2 meV/channel, and the energy resolution, the full width at half-maximum of the zero loss peak (ZLP), was ~18 meV. Individual point spectra have their ZLP maximum aligned at 0 eV and are normalized to the ZLP maximum intensity. The individual spectra of the EELS maps were aligned and then normalized to the maximum value in the selected energy window. Energy windows are 60 meV in width, which is ~3 times the energy resolution of the measurement given by the ZLP full width at half-maximum.

**EELS Simulations.** The electron-driven discrete dipole approximation (e-DDA) was used to carry out all EELS simulations. 55,56 The primary electron beam energy was set to 60 keV, and the impact factors of 2 and 1 nm were chosen for the dimer end and gap position point spectra, respectively. The plane-wave-based near-field enhancements calculated for ITO and silver dimers were performed by using the discrete dipole approximation (DDA).<sup>37</sup> Both ITO and silver dimers were modeled as 20 nm spherical particles with an interdipole target spacing of 0.5 nm and a vacuum background medium with no explicit substrate. The optical constants for silver were taken from ref 45, and the Drude dielectric data for ITO were reported in ref 24. Specifically, the 2% ITO Drude parameters are  $\varepsilon_{\infty}$  = 1.36,  $\hbar \gamma$  = 0.079 eV, and  $\hbar \omega_{v}$  = 0.801 eV, and the 10% ITO Drude parameters are  $\varepsilon_{\infty}$  = 1.41,  $\hbar \gamma$  = 0.179 eV, and  $\hbar\omega_n = 1.48 \text{ eV}.$ 

## ASSOCIATED CONTENT

# **Solution** Supporting Information

The Supporting Information is available free of charge at https://pubs.acs.org/doi/10.1021/acs.jpclett.1c02741.

Additional spectrum images showing the  $\alpha$ ,  $\beta$ ,  $\gamma$ , and  $\delta$  modes of 10% ITO NC dimers; an explanation of the ZLP convolution to the theoretical data in Figure 1 (PDF)

## AUTHOR INFORMATION

## **Corresponding Authors**

David J. Masiello — Department of Materials Science and Engineering and Department of Chemistry, University of Washington, Seattle, Washington 98195, United States; orcid.org/0000-0002-1187-0920; Email: masiello@uw.edu

Jon P. Camden – Department of Chemistry and Biochemistry, University of Notre Dame, Notre Dame, Indiana 46556, United States; orcid.org/0000-0002-6179-2692; Email: jon.camden@nd.edu

## **Authors**

Agust Olafsson — Department of Chemistry and Biochemistry, University of Notre Dame, Notre Dame, Indiana 46556, United States; Occid.org/0000-0001-5252-7881 Siamak Khorasani — Department of Materials Science and Engineering, University of Washington, Seattle, Washington 98195, United States; Occid.org/0000-0003-4395-6910

Jacob A. Busche — Department of Chemistry, University of Washington, Seattle, Washington 98195, United States; orcid.org/0000-0003-4797-9415

Jose J. Araujo — Department of Chemistry, University of Washington, Seattle, Washington 98195, United States; orcid.org/0000-0003-0955-2584

Juan Carlos Idrobo — Center for Nanophase Materials Sciences, Oak Ridge National Laboratory, Oak Ridge, Tennessee 37830, United States; orcid.org/0000-0001-7483-9034

Daniel R. Gamelin — Department of Chemistry, University of Washington, Seattle, Washington 98195, United States; orcid.org/0000-0003-2888-9916

Complete contact information is available at: https://pubs.acs.org/10.1021/acs.jpclett.1c02741

#### Notes

The authors declare no competing financial interest.

## ACKNOWLEDGMENTS

This material is based upon work supported by the Air Force Office of Scientific Research under Award FA9550-21-1-0282. Research at the University of Notre Dame (A.O., J.P.C.) was supported by the Air Force Office of Scientific Research (AFOSR). A.O. was also supported by the HERE program at Oak Ridge National Laboratory and the Patrick and Jana Eilers Graduate Student Fellowship at Notre Dame. Work at the University of Washington was also supported by the AFOSR (S.K., J.A.B., D.J.M.) and by the U.S. National Science Foundation under Award CHE-1904436 (J.J.A., D.R.G.). All STEM experiments were conducted at the Center for Nanophase Materials Sciences, which is a DOE Office of Science User Facility (J.C.I.). This research was conducted, in part, by using instrumentation within ORNL's Materials Characterization Core provided by UT-Battelle, LLC, under Contract DE-AC05-00OR22725 with the DOE, and sponsored by the Laboratory Directed Research and Development Program of Oak Ridge National Laboratory, managed by UT-Battelle, LLC, for the U.S. Department of Energy. Any opinions, findings, and conclusions or recommendations expressed in this material are those of the author(s) and do not necessarily reflect the views of the United States Air Force.

# **■ REFERENCES**

- (1) Maier, S. A. Plasmonics: Fundamentals and Applications; Springer Science & Business Media: 2007.
- (2) Willets, K. A.; Van Duyne, R. P. Localized Surface Plasmon Resonance Spectroscopy and Sensing. *Annu. Rev. Phys. Chem.* **2007**, 58, 267–297.
- (3) Mayer, K. M.; Hafner, J. H. Localized Surface Plasmon Resonance Sensors. *Chem. Rev.* **2011**, *111*, 3828–3857.
- (4) Atwater, H. A.; Polman, A. Plasmonics for improved photovoltaic devices. *Materials for Sustainable Energy* **2010**, *1*–11, 1.
- (5) Jain, P. K.; Huang, X.; El-Sayed, I. H.; El-Sayed, M. A. Noble Metals on the Nanoscale: Optical and Photothermal Properties and Some Applications in Imaging, Sensing, Biology, and Medicine. *Acc. Chem. Res.* **2008**, *41*, 1578–1586.
- (6) Noginov, M. A.; Gu, L.; Livenere, J.; Zhu, G.; Pradhan, A. K.; Mundle, R.; Bahoura, M.; Barnakov, Y. A.; Podolskiy, V. A. Transparent conductive oxides: Plasmonic materials for telecom wavelengths. *Appl. Phys. Lett.* **2011**, *99*, 021101.

- (7) Kim, H.; Osofsky, M.; Prokes, S.; Glembocki, O.; Piqué, A. Optimization of Al-doped ZnO films for low loss plasmonic materials at telecommunication wavelengths. *Appl. Phys. Lett.* **2013**, *102*, 171103.
- (8) Wu, Y.; Wadia, C.; Ma, W.; Sadtler, B.; Alivisatos, A. P. Synthesis and Photovoltaic Application of Copper(I) Sulfide Nanocrystals. *Nano Lett.* **2008**, *8*, 2551–2555.
- (9) Sheldon, M. T.; van de Groep, J.; Brown, A. M.; Polman, A.; Atwater, H. A. Plasmoelectric potentials in metal nanostructures. *Science* **2014**, *346*, 828–831.
- (10) Zhao, B.; Chen, K.; Buddhiraju, S.; Bhatt, G.; Lipson, M.; Fan, S. High-performance near-field thermophotovoltaics for waste heat recovery. *Nano Energy* **2017**, *41*, 344–350.
- (11) Baldassarre, L.; Sakat, E.; Frigerio, J.; Samarelli, A.; Gallacher, K.; Calandrini, E.; Isella, G.; Paul, D. J.; Ortolani, M.; Biagioni, P. Midinfrared Plasmon-Enhanced Spectroscopy with Germanium Antennas on Silicon Substrates. *Nano Lett.* **2015**, *15*, 7225–7231.
- (12) Adato, R.; Yanik, A. A.; Amsden, J. J.; Kaplan, D. L.; Omenetto, F. G.; Hong, M. K.; Erramilli, S.; Altug, H. Ultra-sensitive vibrational spectroscopy of protein monolayers with plasmonic nanoantenna arrays. *Proc. Natl. Acad. Sci. U. S. A.* **2009**, *106*, 19227–19232.
- (13) Valenti, M.; Jonsson, M. P.; Biskos, G.; Schmidt-Ott, A.; Smith, W. A. Plasmonic nanoparticle-semiconductor composites for efficient solar water splitting. *J. Mater. Chem. A* **2016**, *4*, 17891–17912.
- (14) An, L.; Huang, L.; Liu, H.; Xi, P.; Chen, F.; Du, Y. High-Quality Copper Sulfide Nanocrystals with Diverse Shapes and Their Catalysis for Electrochemical Reduction of H<sub>2</sub>O2. Particle & Particle Systems Characterization 2015, 32, 536–541.
- (15) Fang, H.; Hegde, M.; Yin, P.; Radovanovic, P. V. Tuning Plasmon Resonance of In2O3 Nanocrystals throughout the Mid-Infrared Region by Competition between Electron Activation and Trapping. *Chem. Mater.* **2017**, *29*, 4970–4979.
- (16) Schimpf, A. M.; Thakkar, N.; Gunthardt, C. E.; Masiello, D. J.; Gamelin, D. R. Charge-Tunable Quantum Plasmons in Colloidal Semiconductor Nanocrystals. *ACS Nano* **2014**, *8*, 1065–1072.
- (17) Lounis, S. D.; Runnerstrom, E. L.; Llordés, A.; Milliron, D. J. Defect Chemistry and Plasmon Physics of Colloidal Metal Oxide Nanocrystals. *J. Phys. Chem. Lett.* **2014**, *5*, 1564–1574.
- (18) Luther, J. M.; Jain, P. K.; Ewers, T.; Alivisatos, A. P. Localized surface plasmon resonances arising from free carriers in doped quantum dots. *Nat. Mater.* **2011**, *10*, 361–366.
- (19) Gordon, T. R.; Paik, T.; Klein, D. R.; Naik, G. V.; Caglayan, H.; Boltasseva, A.; Murray, C. B. Shape-Dependent Plasmonic Response and Directed Self-Assembly in a New Semiconductor Building Block, Indium-Doped Cadmium Oxide (ICO). *Nano Lett.* **2013**, *13*, 2857–2863.
- (20) Hsu, S.-W.; On, K.; Tao, A. R. Localized Surface Plasmon Resonances of Anisotropic Semiconductor Nanocrystals. *J. Am. Chem. Soc.* **2011**, *133*, 19072–19075.
- (21) Faucheaux, J. A.; Stanton, A. L. D.; Jain, P. K. Plasmon Resonances of Semiconductor Nanocrystals: Physical Principles and New Opportunities. *J. Phys. Chem. Lett.* **2014**, *5*, 976–985.
- (22) Agrawal, A.; Cho, S. H.; Zandi, O.; Ghosh, S.; Johns, R. W.; Milliron, D. J. Localized Surface Plasmon Resonance in Semi-conductor Nanocrystals. *Chem. Rev.* **2018**, *118*, 3121–3207.
- (23) Naik, G. V.; Shalaev, V. M.; Boltasseva, A. Alternative Plasmonic Materials: Beyond Gold and Silver. *Adv. Mater.* **2013**, 25, 3264–3294.
- (24) Olafsson, A.; Busche, J. A.; Araujo, J. J.; Maiti, A.; Idrobo, J. C.; Gamelin, D. R.; Masiello, D. J.; Camden, J. P. Electron Beam Infrared Nano-Ellipsometry of Individual Indium Tin Oxide Nanocrystals. *Nano Lett.* **2020**, *20*, 7987–7994.
- (25) Johns, R. W.; Bechtel, H. A.; Runnerstrom, E. L.; Agrawal, A.; Lounis, S. D.; Milliron, D. J. Direct observation of narrow midinfrared plasmon linewidths of single metal oxide nanocrystals. *Nat. Commun.* **2016**, *7*, 11583.
- (26) Prodan, E.; Radloff, C.; Halas, N. J.; Nordlander, P. A Hybridization Model for the Plasmon Response of Complex Nanostructures. *Science* **2003**, 302, 419–422.

- (27) Quillin, S. C.; Cherqui, C.; Montoni, N. P.; Li, G.; Camden, J. P.; Masiello, D. J. Imaging Plasmon Hybridization in Metal Nanoparticle Aggregates with Electron Energy-Loss Spectroscopy. *J. Phys. Chem. C* 2016, *120*, 20852–20859.
- (28) Cherqui, C.; Li, G.; Busche, J. A.; Quillin, S. C.; Camden, J. P.; Masiello, D. J. Multipolar Nanocube Plasmon Mode-Mixing in Finite Substrates. *J. Phys. Chem. Lett.* **2018**, *9*, 504–512.
- (29) Yankovich, A. B.; Munkhbat, B.; Baranov, D. G.; Cuadra, J.; Olsén, E.; Lourenço-Martins, H.; Tizei, L. H. G.; Kociak, M.; Olsson, E.; Shegai, T. Visualizing Spatial Variations of Plasmon–Exciton Polaritons at the Nanoscale Using Electron Microscopy. *Nano Lett.* **2019**, *19*, 8171–8181.
- (30) Tizei, L. H. G.; Mkhitaryan, V.; Lourenço-Martins, H.; Scarabelli, L.; Watanabe, K.; Taniguchi, T.; Tencé, M.; Blazit, J.-D.; Li, X.; Gloter, A.; et al. Tailored Nanoscale Plasmon-Enhanced Vibrational Electron Spectroscopy. *Nano Lett.* **2020**, *20*, 2973–2979.
- (31) Prodan, E.; Nordlander, P. Plasmon hybridization in spherical nanoparticles. *J. Chem. Phys.* **2004**, *120*, 5444–5454.
- (32) Koh, A. L.; Bao, K.; Khan, I.; Smith, W. E.; Kothleitner, G.; Nordlander, P.; Maier, S. A.; McComb, D. W. Electron Energy-Loss Spectroscopy (EELS) of Surface Plasmons in Single Silver Nanoparticles and Dimers: Influence of Beam Damage and Mapping of Dark Modes. *ACS Nano* **2009**, *3*, 3015–3022.
- (33) Cho, S. H.; Roccapriore, K. M.; Dass, C. K.; Ghosh, S.; Choi, J.; Noh, J.; Reimnitz, L. C.; Heo, S.; Kim, K.; Xie, K.; et al. Spectrally tunable infrared plasmonic F,Sn:In2O3 nanocrystal cubes. *J. Chem. Phys.* **2020**, *152*, 014709.
- (34) Xi, M.; Reinhard, B. M. Localized Surface Plasmon Coupling between Mid-IR-Resonant ITO Nanocrystals. *J. Phys. Chem. C* **2018**, 122, 5698–5704.
- (35) Agrawal, A.; Singh, A.; Yazdi, S.; Singh, A.; Ong, G. K.; Bustillo, K.; Johns, R. W.; Ringe, E.; Milliron, D. J. Resonant Coupling between Molecular Vibrations and Localized Surface Plasmon Resonance of Faceted Metal Oxide Nanocrystals. *Nano Lett.* **2017**, *17*, 2611–2620.
- (36) Wu, Y.; Li, G.; Camden, J. P. Probing Nanoparticle Plasmons with Electron Energy Loss Spectroscopy. *Chem. Rev.* **2018**, *118*, 2994–3031.
- (37) Cherqui, C.; Thakkar, N.; Li, G.; Camden, J. P.; Masiello, D. J. Characterizing Localized Surface Plasmons Using Electron Energy-Loss Spectroscopy. *Annu. Rev. Phys. Chem.* **2016**, *67*, 331–357.
- (38) Krivanek, O. L.; Lovejoy, T. C.; Dellby, N.; Aoki, T.; Carpenter, R. W.; Rez, P.; Soignard, E.; Zhu, J.; Batson, P. E.; Lagos, M. J.; et al. Vibrational spectroscopy in the electron microscope. *Nature* **2014**, *514*, 209–212.
- (39) Hachtel, J. A.; Lupini, A. R.; Idrobo, J. C. Exploring the capabilities of monochromated electron energy loss spectroscopy in the infrared regime. *Sci. Rep.* **2018**, *8*, 5637.
- (40) Lovejoy, T.; Corbin, G.; Dellby, N.; Hoffman, M.; Krivanek, O. Advances in Ultra-High Energy Resolution STEM-EELS. *Microsc. Microanal.* **2018**, 24, 446–447.
- (41) Cho, S. H.; Ghosh, S.; Berkson, Z. J.; Hachtel, J. A.; Shi, J.; Zhao, X.; Reimnitz, L. C.; Dahlman, C. J.; Ho, Y.; Yang, A.; et al. Syntheses of Colloidal F:In2O3 Cubes: Fluorine-Induced Faceting and Infrared Plasmonic Response. *Chem. Mater.* **2019**, *31*, 2661–2676.
- (42) Rosen, E. L.; Buonsanti, R.; Llordes, A.; Sawvel, A. M.; Milliron, D. J.; Helms, B. A. Exceptionally Mild Reactive Stripping of Native Ligands from Nanocrystal Surfaces by Using Meerwein's Salt. *Angew. Chem., Int. Ed.* **2012**, *51*, 684–689.
- (43) Smith, K. C.; Olafsson, A.; Hu, X.; Quillin, S. C.; Idrobo, J. C.; Collette, R.; Rack, P. D.; Camden, J. P.; Masiello, D. J. Direct Observation of Infrared Plasmonic Fano Antiresonances by a Nanoscale Electron Probe. *Phys. Rev. Lett.* **2019**, *123*, 177401.
- (44) Egerton, R. F. Electron Energy-Loss Spectroscopy in the Electron Microscope; Springer Science & Business Media: 2011.
- (45) Johnson, P. B.; Christy, R. W. Optical Constants of the Noble Metals. *Phys. Rev. B* **1972**, *6*, 4370–4379.

- (46) Cahill, K. Models of membrane electrostatics. *Phys. Rev. E* 2012, 85, 051921.
- (47) Kadkhodazadeh, S.; Christensen, T.; Beleggia, M.; Mortensen, N. A.; Wagner, J. B. The Substrate Effect in Electron Energy-Loss Spectroscopy of Localized Surface Plasmons in Gold and Silver Nanoparticles. *ACS Photonics* **2017**, *4*, 251–261.
- (48) Kadkhodazadeh, S.; de Lasson, J. R.; Beleggia, M.; Kneipp, H.; Wagner, J. B.; Kneipp, K. Scaling of the Surface Plasmon Resonance in Gold and Silver Dimers Probed by EELS. J. Phys. Chem. C 2014, 118, 5478–5485.
- (49) Kalinin, S. V.; Roccapriore, K. M.; Cho, S. H.; Milliron, D. J.; Vasudevan, R.; Ziatdinov, M.; Hachtel, J. A. Separating Physically Distinct Mechanisms in Complex Infrared Plasmonic Nanostructures via Machine Learning Enhanced Electron Energy Loss Spectroscopy. *Adv. Opt. Mater.* 2021, *9*, 2001808.
- (50) Kuznetsov, A. S. Effect of proximity in arrays of plasmonic nanoantennas on hot spots density: Degenerate semiconductors vs. conventional metals. *Plasmonics* **2016**, *11*, 1487–1493.
- (51) Cherqui, C.; Bigelow, N. W.; Vaschillo, A.; Goldwyn, H.; Masiello, D. J. Combined Tight-Binding and Numerical Electrodynamics Understanding of the STEM/EELS Magneto-optical Responses of Aromatic Plasmon-Supporting Metal Oligomers. ACS Photonics 2014, 1, 1013–1024.
- (52) Jansons, A. W.; Hutchison, J. E. Continuous Growth of Metal Oxide Nanocrystals: Enhanced Control of Nanocrystal Size and Radial Dopant Distribution. *ACS Nano* **2016**, *10*, 6942–6951.
- (53) Crockett, B. M.; Jansons, A. W.; Koskela, K. M.; Johnson, D. W.; Hutchison, J. E. Radial Dopant Placement for Tuning Plasmonic Properties in Metal Oxide Nanocrystals. *ACS Nano* **2017**, *11*, 7719–7728
- (54) Staller, C. M.; Robinson, Z. L.; Agrawal, A.; Gibbs, S. L.; Greenberg, B. L.; Lounis, S. D.; Kortshagen, U. R.; Milliron, D. J. Tuning Nanocrystal Surface Depletion by Controlling Dopant Distribution as a Route Toward Enhanced Film Conductivity. *Nano Lett.* **2018**, *18*, 2870–2878.
- (55) Bigelow, N. W.; Vaschillo, A.; Iberi, V.; Camden, J. P.; Masiello, D. J. Characterization of the Electron- and Photon-Driven Plasmonic Excitations of Metal Nanorods. *ACS Nano* **2012**, *6*, 7497–7504.
- (56) Bigelow, N. W.; Vaschillo, A.; Camden, J. P.; Masiello, D. J. Signatures of Fano Interferences in the Electron Energy Loss Spectroscopy and Cathodoluminescence of Symmetry-Broken Nanorod Dimers. ACS Nano 2013, 7, 4511–4519.
- (57) Draine, B. T.; Flatau, P. J. Discrete-Dipole Approximation For Scattering Calculations. *J. Opt. Soc. Am. A* **1994**, *11*, 1491–1499.